

Effect of Strain on Microstructure Evolution of 1Cr18Ni9Ti Stainless Steel During Adiabatic Shearing

Y. Yang, L.H. Jiang, S.H. Luo, H.B. Hu, T.G. Tang, and Q.M. Zhang

(Submitted July 27, 2015; in revised form October 12, 2015; published online December 1, 2015)

Dynamic shear test was conducted on the hat-shaped specimen of the thermo-mechanical-processed 1Cr18Ni9Ti stainless steel by using the split Hopkinson pressure bar at ambient temperature. The effect of the shear strain on the microstructure evolution was investigated during adiabatic shearing. The results revealed that the development of adiabatic shear localization went through three stages, including the incubation period, the development stage, and the maturity period. TEM observations showed that the grains in the shear region were elongated, and the elongated grains were gradually evolved into equiaxed nano-grains of 100 nm as shear strain increased. The rotational dynamic recrystallization kinetics calculation showed that subgrains had sufficient time to generate an equiaxed microcrystalline structure by rotation within the deformation time. Based on the observation of the evolution of dislocations and subgrains in the adiabatic shear region, a model of the microstructure evolution was established during the adiabatic shearing.

Keywords adiabatic shearing, microstructure evolution, split Hopkinson pressure bar, stainless steel

1. Introduction

Adiabatic shearing is a common form of localized plastic deformation under high strain rate, and frequently appears at the high strain rate deformation involving the impact loading, such as, high-speed impact, penetration, erosion, high speed cutting, high-speed molding, and explosive cladding (Ref 1-3). The adiabatic shear bands (ASBs) have been observed in titanium alloy (Ref 4, 5), aluminum alloy (Ref 6, 7), and steel (Ref 8-10). The strain rate is so high (up to 10^3 - 10^7 /s) and the deformation time is very short during adiabatic shearing. Thus, it is difficult to observe microstructure evolution process during adiabatic shearing. Researchers can only speculate a corresponding microstructure evolution process during adiabatic shearing with the observed final microstructure.

Andrade et al. (Ref 11) analyzed the microstructure of ASB in copper by using TEM and diffraction analysis. He found that there were nano-grains in the center of ASB, and the diffraction pattern was closer to the ring-like as the grains got towards the

center of ASB, which indicated that these small equiaxed grains had large misorientation, and the process was owed to the dynamic recrystallization. RDR mechanism was proposed by Meyers et al. (Ref 8) and was validated by Yang (Ref 3, 12) in the titanium alloy and 7075 aluminum alloy. Xue et al. (Ref 9, 13, 14) studied the development of ASB and the microstructure characteristics of post-shear localization in cold-rolled 316L stainless steel, and pointed out that well-developed shear bands were comprised with a mixture of equiaxed, rectangular, and elongated sub-grains. Dynamic or static recovery and continuous dynamic recrystallization were thought to be the main mechanisms for the substructures formed inside the shear bands. Meyers et al. (Ref 8, 9) studied the microstructure characteristics of ASBs in austenitic stainless steel. However, the effect of strain on the microstructure evolution during adiabatic shearing has been rarely reported.

The microstructure evolution of 1Cr18Ni9Ti austenitic stainless steel with different shear strains during adiabatic shearing was studied in the present work.

2. Experiments

Table 1 shows the chemical composition of 1Cr18Ni9Ti stainless steel used in this work. The as-received material was annealed in the ammonia decomposition furnace at the temperature of 1323 K for 50 min, then water quenched, following cold rolled (total 5% deformation), and annealed in inert gases at 1198 K for 72 h and finally water quenched.

The hat-shaped specimens of the 1Cr18Ni9Ti stainless steel were dynamically compressed by using a split Hopkinson pressure bar (SHPB). The material of the incidental bar, the transmission bar, and the striker bar of the SHPB are all martensitic steels, and they all have the same diameters of 14.5 mm. The length of the incidental bar, the transmission bar, and the striker bar are 1200, 1000, and 200 mm, respectively. The apparatus figure is schematically showed in Fig. 1(a). Hat-shaped specimens were used to generate high shear strains in a localized region. The stop ring with different heights of 0.9,

Y. Yang, School of Material Science and Engineering, Central South University, Changsha 410083, China; Institute of Fluid Physics, Chinese Academy of Engineering Physics, Mianyang 621900, China; State Key Laboratory of Explosion Science and Technology, Beijing Institute of Technology, Beijing 100081, China; and Key Laboratory of Ministry of Education for Nonferrous Metal Materials Science and Engineering, Central South University, Changsha 410083, China; **L.H. Jiang** and **S.H. Luo**, School of Material Science and Engineering, Central South University, Changsha 410083, China; **H.B. Hu** and **T.G. Tang**, Institute of Fluid Physics, Chinese Academy of Engineering Physics, Mianyang 621900, China; and **Q.M. Zhang**, State Key Laboratory of Explosion Science and Technology, Beijing Institute of Technology, Beijing 100081, China. Contact e-mail: yangyang@csu.edu.cn.

Table 1 Chemical composition of 1Cr18Ni9Ti stainless steel

Element	C	Si	Mn	P	S	Ni	Cr	Mo	other
Content (wt/%)	≤ 0.12	≤ 1.00	≤ 2.00	≤ 0.035	≤ 0.030	8.00-11.00	17.00-19.00	...	Ti 5*(C%-0.02)-0.80

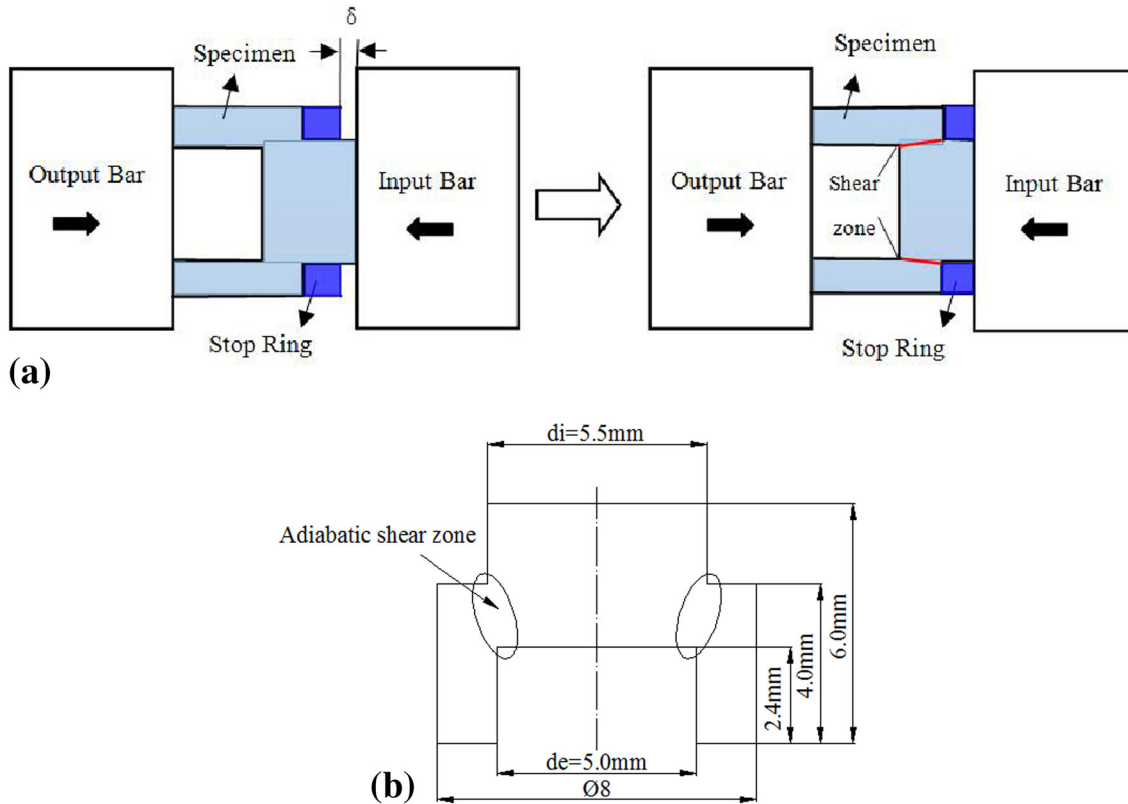


Fig. 1 Schematic diagram of SHPB test. (a) SHPB, (b) hat-shaped specimen

1.1, and 1.5 mm was used to control the shear strains of the hat-shaped specimens. Thus, the displacements of the hat-shaped specimens were controlled and they were 1.1, 0.9, and 0.5 mm, respectively. Consequently, the adiabatic shear deformation of hat-shaped specimens will be “frozen” in different stages during the development of ASBs. The deformation process of hat-shaped specimen was considered as the cylinder compressive process. And the nominal shear strain (γ) can be calculated from the following formula (Ref 15):

$$\gamma = \delta/x \quad (\text{Eq 1})$$

where δ is the displacements (or compression reduction) of the hat-shaped specimen; $x = (d_i - d_e)/2$, d_i and d_e are the dimensions of hat-shaped specimen, as shown in Fig. 1(b). The calculated nominal shear strains are 2.0, 3.6, and 4.4, respectively. Figure 1(a) illustrates the process of adiabatic shear deformation. The specimen was loaded at 293 K in this work.

According to the following equations (Ref 5), the electrical signals during the adiabatic shear deformation would be converted into true stress-strain curve:

$$\tau(t) = \frac{E_0 d_i^2 e_r(t)}{L(d_i + d_e)} \quad (\text{Eq 2})$$

$$\dot{\gamma} = \frac{2C_0 e_r(t)}{W} \quad (\text{Eq 3})$$

$$\gamma(t) = \int_0^t \dot{\gamma}(t) dt \quad (\text{Eq 4})$$

$$\varepsilon = \ln \sqrt{1 + \gamma + \frac{\gamma^2}{2}} \quad (\text{Eq 5})$$

where E_0 is the elastic modulus of steel ($E_0 = 200\text{ GPa}$), C_0 is the longitudinal wave velocity ($C_0 = 5000\text{ m/s}$), L and W are the length and width of the shear band, d_i and d_e are the geometrical parameters of the hat-shaped specimen, as shown in Fig. 1(b), and $e_r(t)$ and $e_t(t)$ are strain of reflected and transmitted stress pulse on the split Hopkinson pressure bars.

The optical metallographic microscopes of the specimens were observed with POLYVAR-MET. The chemical attack for specimens was a solution of 20 mL HF + 10 mL HNO₃ + 70 mL H₂O. After hand-grinding, the sample was reduced to a thickness of about 50 μm , and then the foils were perforated upon the shear band by ion thinning in Gatan 691 Ion Milling at 243 K. TEM observations were carried out with a FEI Tecnai F30 transmission electron microscope and were operated at 300 kV.

3. Results and Discussion

3.1 Dynamic Stress-Strain Response and Thermal-Mechanical Parameters in the Shear Region

The starting time for ASB formation was just the instant when the strain rate reached the first vibration peak of reflection signal, and ended with last vibration peak of transmission signal (Ref 13). The strain rate within the shear band can be determined from Eq 3. The relation between the true flow stress and true strain in the shear region is shown in Fig. 2, which was obtained by using Eq 2-5.

The average strain rate during adiabatic shear deformation can be calculated from Fig. 2(a). It is about 5.0×10^5 and $5.2 \times 10^5/s$ corresponding to the nominal shear strain of 3.6 and 4.4, respectively, which are extremely high in comparison with 10^{-3} - $10^{-1}/s$ during quasi-static deformation. The true stress-strain curve of specimens is shown in Fig. 2(b). And the curve illustrates the adiabatic shear characteristic of the stainless steel. It can be divided into three parts: first, the true flow stress increases with the strain hardening; then the true flow stress changes with small fluctuation as the strain hardening and thermal softening reach equilibrium. The highest true stress reached 1205 and 1402 MPa, respectively; the thermal softening effect exceeded the strain and strain rate hardening, which resulted in the thermo-visco-plastic instability, and then the ASB was formed.

The adiabatic temperature rise in ASB is a significant parameter for the formation of an ASB and the microstructure evolution. When the strain rate is greater than $10^3/s$, the deformation process of the whole shear area can be considered as the adiabatic deformation. As calculated above, the average strain rate is as high as $5.0 \times 10^5/s$; thus, adiabatic temperature rise can be calculated by following equations (Ref 16):

$$T_i = T_0 + \frac{\eta}{\rho C_v} S_i \quad (\text{Eq 6})$$

$$S_i = \frac{\Delta \varepsilon_i \times (\sigma_i + \sigma_{(i+1)})}{2} \quad (i = 1, 2, 3 \dots) \quad (\text{Eq 7})$$

where T_0 , ρ , C_v , η , γ , and σ are room temperature, the density, heat capacity, work to heat conversion coefficient, strain, and flow stress, respectively. For 1Cr18Ni9Ti stainless steel,

$C_v = 500 \text{ J/(kg}\cdot\text{K)}$ (Ref 17), $\rho = 7850 \text{ kg/m}^3$. Generally, the work to heat conversion coefficient η is 0.9. Here, $T_0 = 293 \text{ K}$.

S_i is the plastic work per unit area. The dynamic response data in the shear band shown in Fig. 2(b) can be divided into lots of continuous blocks with strain increment, and the area of each block (S_i) can be calculated by Eq 6. The temperature-time curve can be constructed by substituting S_i into Eq 6, as shown in Fig. 3. It should be noticed that the maximum adiabatic temperature rise of the nominal shear strain $\gamma = 3.6$ and 4.4 are 954 and 985 K, respectively.

3.2 Microstructure Characteristics with Different Nominal Shear Strains

As shown in Fig. 4(a), the grains in the unloaded specimen were quite large with size of $\sim 280 \mu\text{m}$, and the annealing twins were less. The metallograph of specimens loaded by SHPB are shown in Fig. 4(b)-(d). ASB began to nucleate from the specimen geometric position, and then gradually extended inward. With the increase of nominal shear strain, the shear region gradually becomes clear, and the ASB width increases constantly. The width value of ASB measured through optical

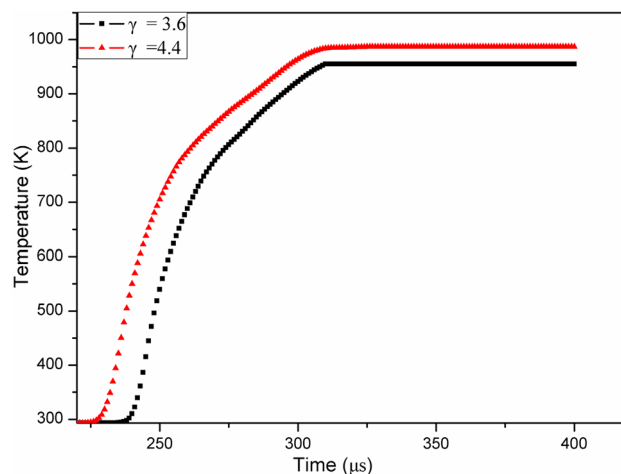


Fig. 3 Adiabatic temperature rise as a function of time

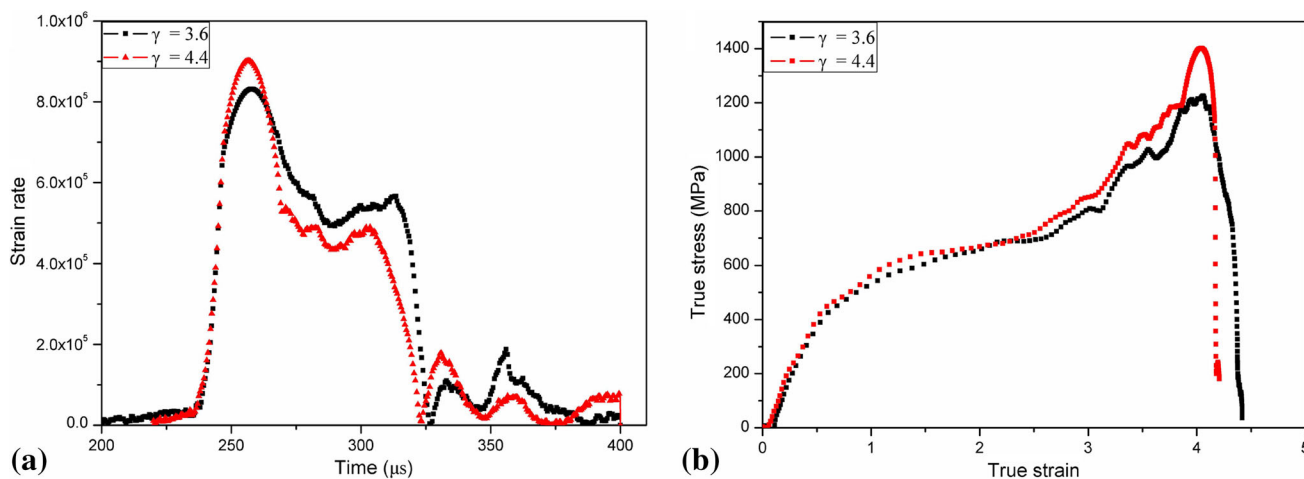


Fig. 2 (a) Strain rate-time curve; (b) true stress-strain curve with nominal shear strain of 3.6 and 4.4

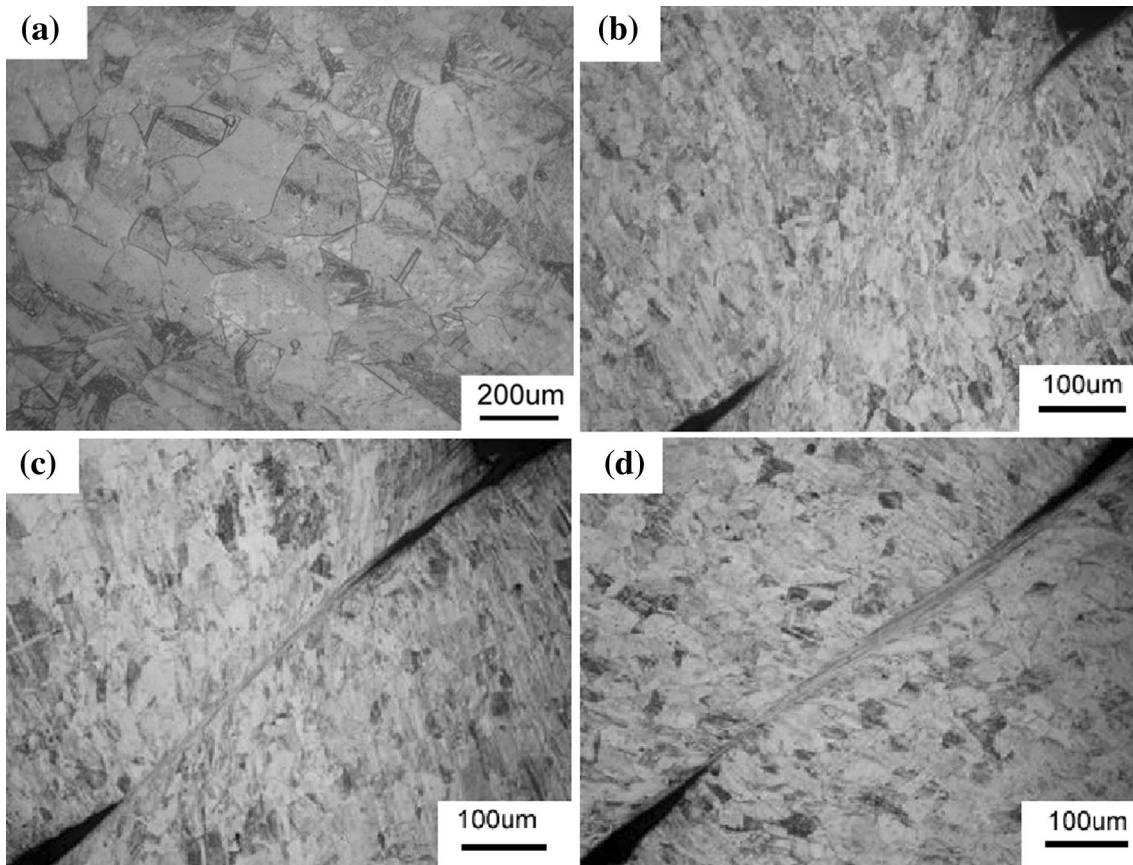


Fig. 4 Optical micrograph of specimens (a) specimen before loading; specimens after loading with nominal shear strain of 2.0, 3.6, 4.4 are (b), (c), (d), respectively

Table 2 ASB width of specimen with different nominal shear strains

Nominal shear strain γ	ASB width (μm)
2.0	0
3.6	15.4
4.4	18.7

microscopy (OM) is listed in Table 2. Combined with Fig. 4 and Table 2, it can be determined qualitatively that the specimens with nominal shear strain of 2.0, 3.6, and 4.4 were at the three stages, which were the initial stage, the development period, and the maturity period, respectively.

Figure 5 shows the TEM morphology of the specimen with the nominal shear strain of 2.0. Figure 5(a) is the bright field image of the shear region and the corresponding selected area electron diffraction pattern (SAED). Combined with the dark field image (Fig. 5b), it was confirmed that the grains were elongated austenite in the shear region. The short axis width of the elongated grains was about 110 nm. And the corresponding SAED was proved to be a single crystal diffraction pattern. Twins were observed in the matrix near the shear area (Fig. 5c), and corresponding SAED is shown in Fig. 5(d).

Figure 6 shows the TEM morphology of the specimen with nominal shear strain of 3.6. Figure 6(a) is the bright field image of the shear region at the development stage. Combined with

the dark field image (Fig. 6b), it can be observed that some equiaxed subgrains appeared among the elongated austenite grains in the shear band, and the dislocation density in subgrains was also much higher. The short axis width of the elongated grains was about 100 nm. As compared with Figs. 5(a) and 6(a), it can be seen that the short axis width of elongated austenite grains decreased with the increase of nominal shear strain. As seen in Fig. 6(c), the corresponding SAED was a discontinuous ring, meaning that there existed a large number of elongated grains in the shear band, and part of which were split into sub-grains with large misorientation.

The average strain rate of the specimen with nominal shear strains of 3.6 was $5.0 \times 10^5/\text{s}$ and the maximum of true stress reached 1205 MPa, which provided suitable conditions for the adiabatic shear deformation. Figure 3 shows that the adiabatic temperature rise reached 954 K ($0.55T_m$, $T_m = 1713$ K), which was higher than the recrystallization temperature of austenite stainless steel ($0.4-0.5T_m$), that provided temperature condition for the dynamic recrystallization in ASB.

Figure 7 shows the TEM morphology of the specimen with nominal shear strain of 4.4. Figure 7(a) is the bright field image of the shear region in mature stage. Combined with the dark field image (Fig. 7b), it can be observed that equiaxed subgrains with size of about 100 nm appeared among the shear band, and the dislocation density in subgrains was still high. The short axis width of elongated grains was about 100 nm, just the same as the specimen with nominal shear strains of 3.6. The short axis width of elongated grains decreased with the increase of nominal shear strain and finally

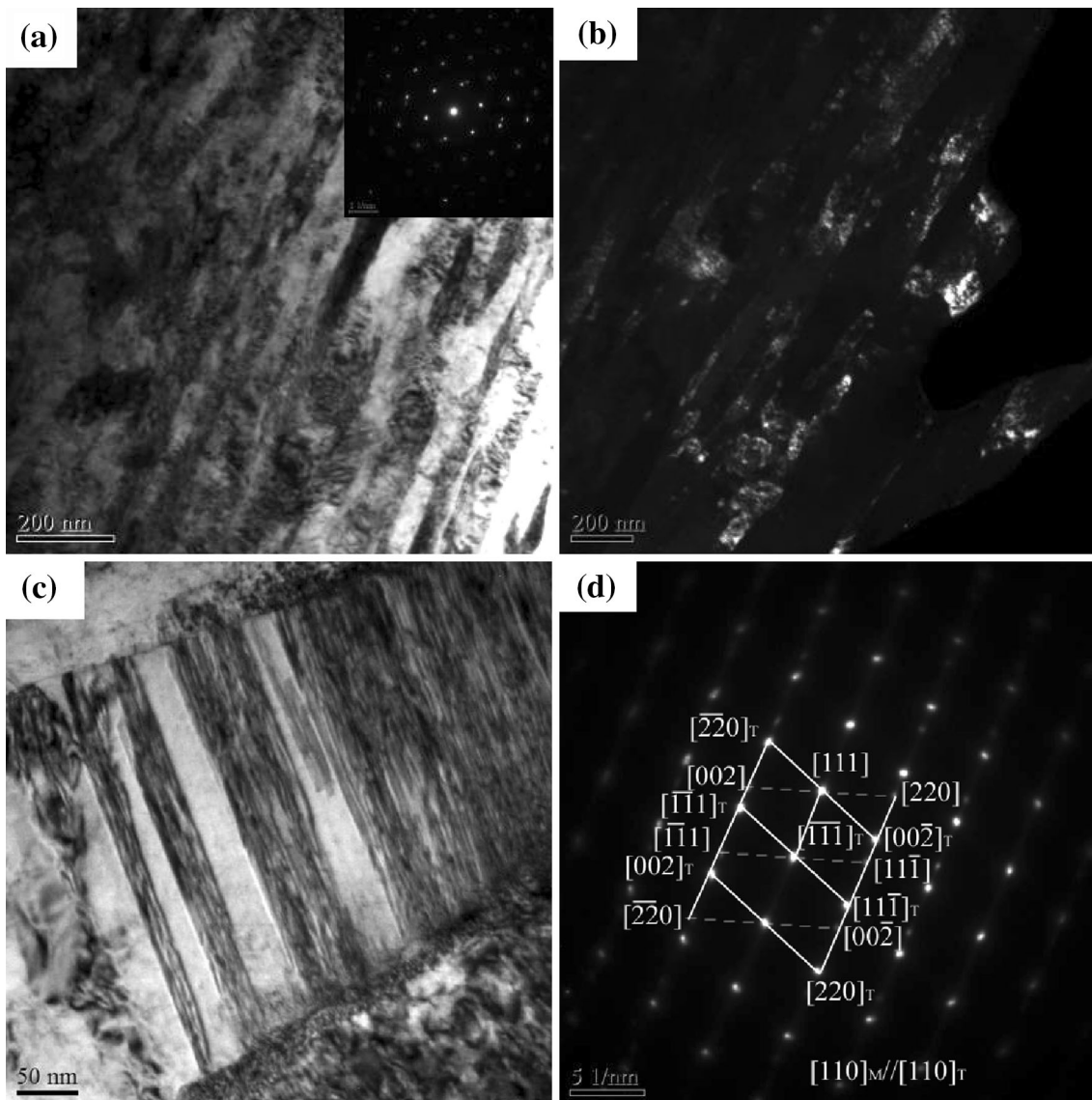


Fig. 5 Adiabatic shear morphology of specimen with the nominal shear strain $\gamma = 2.0$. (a) the bright field image and the corresponding SAED pattern; (b) the corresponding dark field image; (c) the twins in the matrix near the shear area; (d) the corresponding SAED pattern of twins

reached about 100 nm as compared with Figs. 5(a) and (b), 6(a) and (b), 7(a) and (b). And the equiaxed grain has the same grain morphology of dynamic recrystallization. The corresponding SAED (Fig. 7c) was polycrystalline diffraction pattern, and was more continuous than that with nominal shear strain of 3.6 (Fig. 6c). It indicated that when nominal shear strain reached 4.4, the grains were much finer than those of the specimens with nominal shear strain of 2.0 and 3.6. And a large number of fine grains with high-angle boundary were observed in ASB.

The average strain rate of the specimen with nominal shear strains of 4.4 was $5.2 \times 10^5/s$, as shown in Fig. 2, and the maximum of true stress reached 1402 MPa, which provided conditions for the adiabatic shear deformation. Figure 3 shows that adiabatic temperature rise reached 985 K ($0.57T_m$), which was higher than the recrystallization temperature of austenite stainless steel ($0.4-0.5T_m$), providing the temperature condition for the dynamic recrystallization in ASB.

3.3 Kinetics Calculation for Formation of the Nanograins by RDR Mechanism

The microstructure within the adiabatic shear zone (as shown in Fig. 4) has similar equiaxed nanograins to the characterization of various materials during dynamic shearing. The classical recrystallization mechanisms, such as the high-angle grain boundary migration mechanism and the sub-grains coalescence mechanism cannot explain the possibility of the instant and sharp refinement of grains in kinetics. They are at least 3 to 4 orders of magnitude slower than the adiabatic temperature curve. In response to this question, scholars have proposed multiple kinds of new mechanism for dynamic recrystallization. However, it is now widely recognized that RDR mechanism proposed by Meyers et al. (Ref 8) is more reasonable in kinetics. The recrystallized grains were formed by the driving force of interface energy, which was described as the following equations (Ref 8):

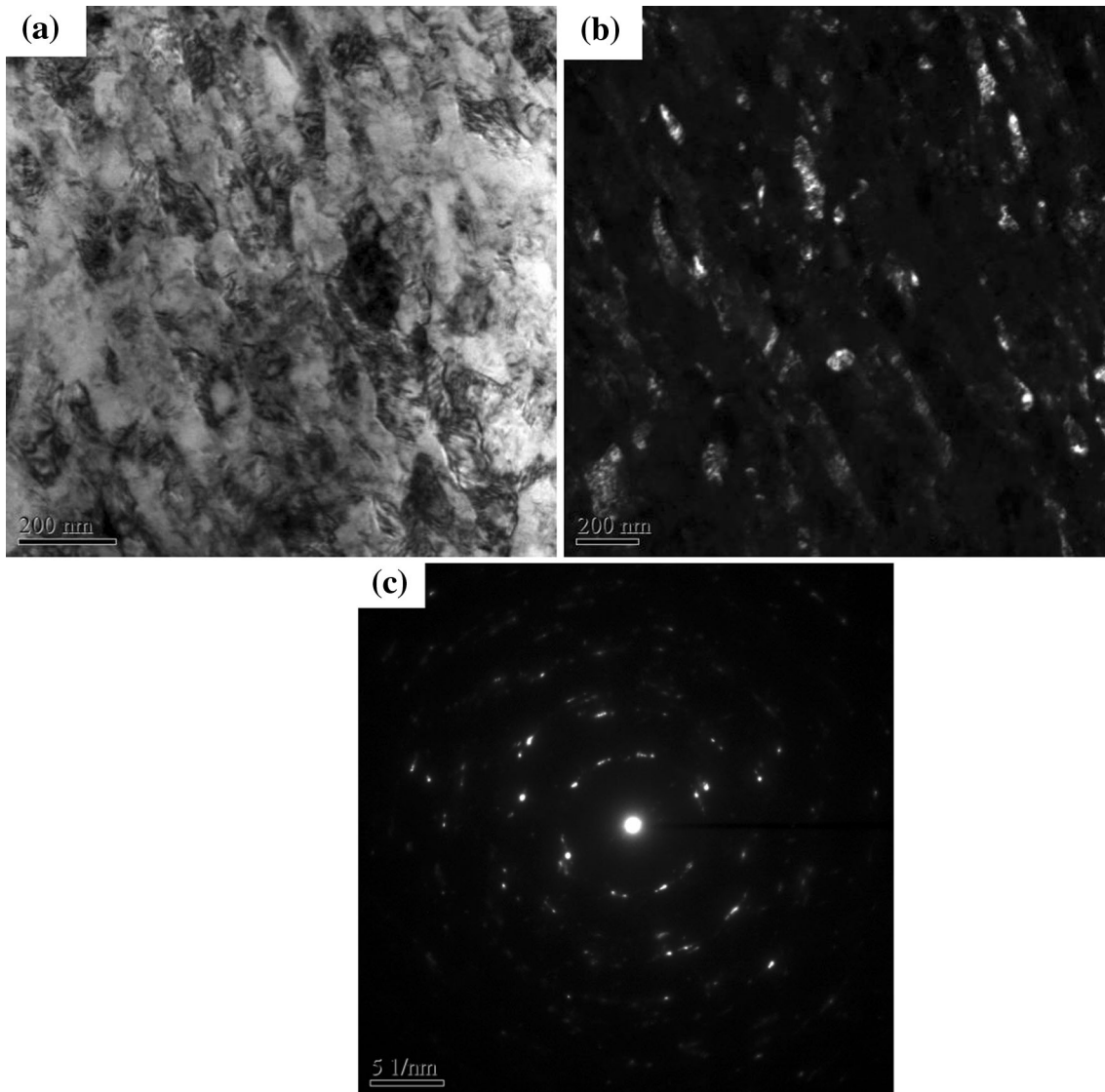


Fig. 6 Adiabatic shear morphology of specimen with the nominal shear strain $\gamma = 3.6$. (a) the bright field image (b) the corresponding dark field image; (c) the corresponding SAED pattern

$$t = \frac{L_1 K T f(\theta)}{4 \delta \eta D} = \frac{L_1 K T f(\theta)}{4 \delta \eta D_0 \exp(-Q_b/RT)} \quad (\text{Eq 8})$$

$$f(\theta) = \frac{3 \tan(\theta) - 2 \cos(\theta)}{3 - 6 \sin(\theta)} - \frac{4\sqrt{3}}{9} \ln \frac{2 + \sqrt{3}}{2 - \sqrt{3}} + \frac{4\sqrt{3}}{9} \ln \frac{\tan(\theta/2) - 2 - \sqrt{3}}{\tan(\theta/2) - 2 + \sqrt{3}} + \frac{2}{3} \quad (\text{Eq 9})$$

where t is the time of dynamic recrystallization, T is the temperature, δ is the thickness of grain boundaries, η is the grain boundaries energy, and D_0 is a constant associated with grain boundary diffusion. L_1 is the average size of subgrains (0.1 μm), Q_b is the diffusion activation energy of solute atoms, and θ is the subgrain misorientation. In this work, the parameters used in Eq 8 are $\delta = 0.5$ nm (Ref 8), $\eta = 0.625$ J/m² (Ref 8), $D_0 = 7.8 \times 10^{-5}$ m/s (Ref 8), $Q_b = 167$ kJ/mol (Ref 8), $k = 1.38 \times 10^{-23}$ J/K, $R = 8.314$ J/mol.

According to RDR mechanism, the grain boundaries need to rotate about 0.523 radians (30°) to form recrystallized grains. The refined grain was caused by the rotation of subgrain boundaries.

The value of θ ranges from 0° to 30°. The combination of above equations can get the results, and different grain sizes under different temperatures are executed by recrystallization kinetic calculation. Figure 8(a) shows the time of forming refined grains with an average grain size of 100 nm when temperature varied from 0.45 T_m to 0.55 T_m . Figure 8(b) shows the time of forming average grain size, which varied from 100 to 300 nm at 0.55 T_m . According to the calculation results, the time of forming refined grains with an average size of 100 and 300 nm were only finished in 20 and 60 μs , respectively. The lower the temperature is, the more time is needed to form the same size grains, while under the same temperature, the larger the formed grains, the more time is needed. According to Fig. 2(a), the entire adiabatic shear deformation time sustained about 90.7 μs . That was to say, there were enough time for broken grains to form equiaxed nano-grains through the rotation of subgrains. Therefore, for the formation of equiaxed grains with size of 100 nm within the adiabatic shear zone in the present work, RDR mechanism can well explain the possibility of instant (within about 90.7 μs) and sharp refinement of grains size in kinetics.

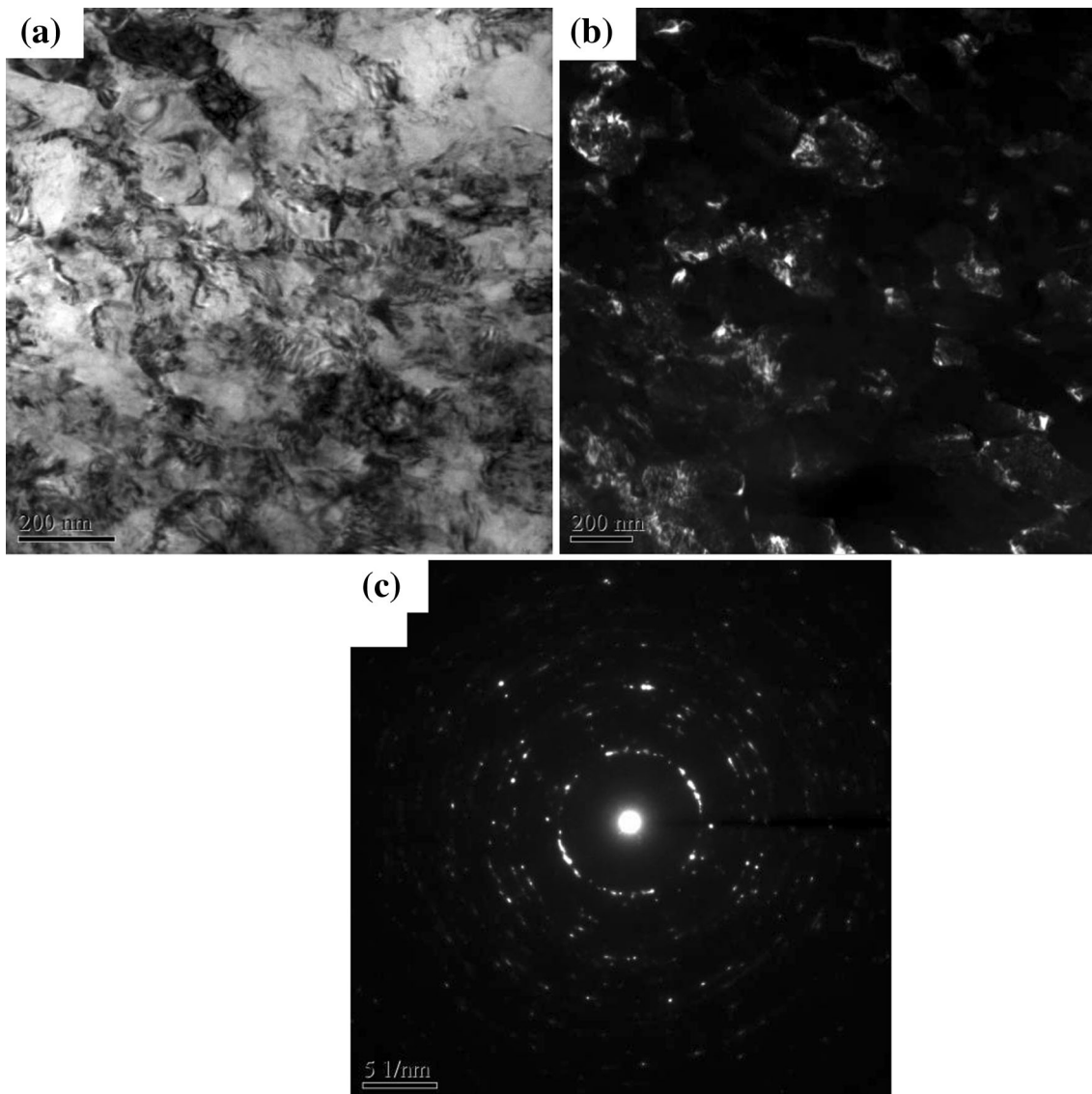


Fig. 7 Adiabatic shear morphology of specimen under the nominal shear strain $\gamma = 4.4$. (a) the bright field image (b) the corresponding dark field image; (c) the corresponding SAED pattern

3.4 Effect of Nominal Shear Strain on Microstructure Evolution Within the Adiabatic Shear Zone

Effect of nominal shear strain on adiabatic shear deformation was mainly reflected in the degree of shear deformation, adiabatic temperature rise, and the grains and dislocations configurations within the shear zone.

It is obviously observed that the strain effect enhanced with the increase of shear strain (Fig. 2a). It can be concluded that the higher the strain was, the higher the adiabatic temperature rise was. According to Fig. 2, the average strain rate in ASB was 5.0×10^5 and 5.2×10^5 /s at nominal shear strain of 3.6 and 4.4, respectively, which were much higher than that under the strain rate of 10^{-3} /s quasi-static. However, according to Fig. 3, the adiabatic temperature rise within ASB was 954 and 985 K at the nominal shear strain of 3.6 and 4.4, respectively, which were higher than the recrystallization temperature of the stainless steel ($0.4-0.5T_m$, $T_m = 1731$ K).

Specimens would be kept in different adiabatic shearing stages under different nominal shear strains loading (as shown

in Fig. 4). Grains in the shear region were elongated along the direction of shear deformation and the dislocations density had a sharp increase at the initial stage ($\gamma = 2.0$) (shown in Fig. 5a). With the increase of nominal shear strain ($\gamma = 3.6$), the austenite grains were kept elongated along the direction of shear deformation, and sub-grains with high dislocation density were produced in these elongated austenite grains within ASB (Fig. 6a). When the nominal shear strain was up to 4.4, most elongated grains in ASB disappeared and were replaced by equiaxed grains of an average size of 100 nm (Fig. 7a). Those equiaxed grains with high dislocation density were produced through RDR.

Considering the effects of shear strain on microstructure evolution during adiabatic shear localization, it can be concluded that original specimen contained coarse grains and had a low dislocation density. As the nominal shear strain increased (e.g., 2.0), grains in shear region were elongated along shear direction and dislocation density where dislocation tangles or cells were formed increased sharply. With further increase of

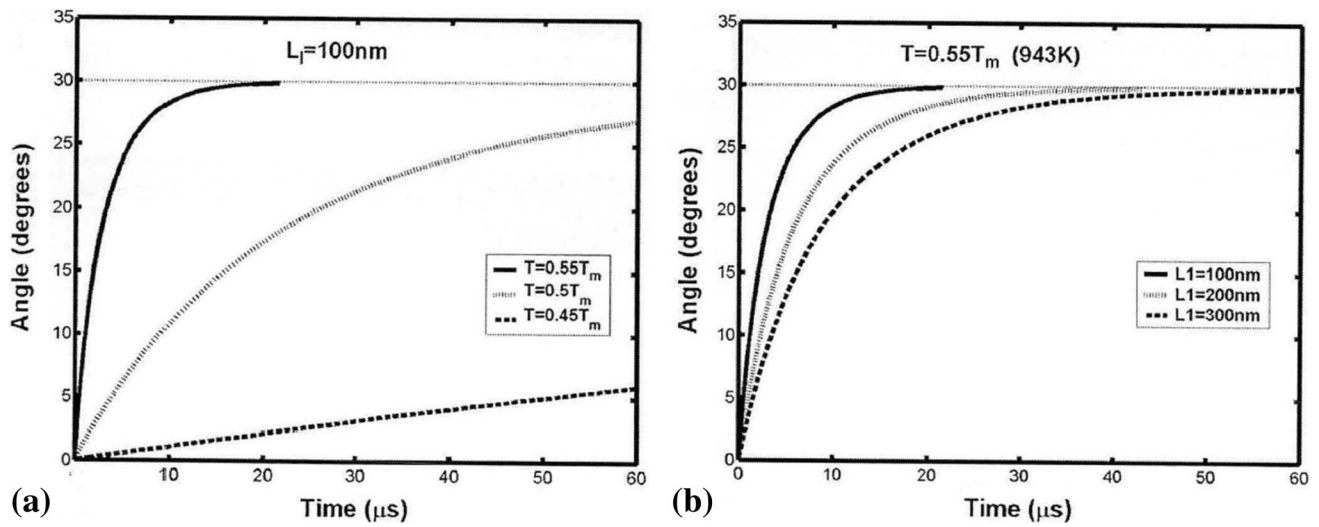


Fig. 8 The kinetic curves of equiaxed grains produced by the rotation of subgrain boundaries. (a) The time of producing grains with average size of 100 nm at different temperatures (b) the time of producing different grain sizes at the temperature of $0.55T_m$

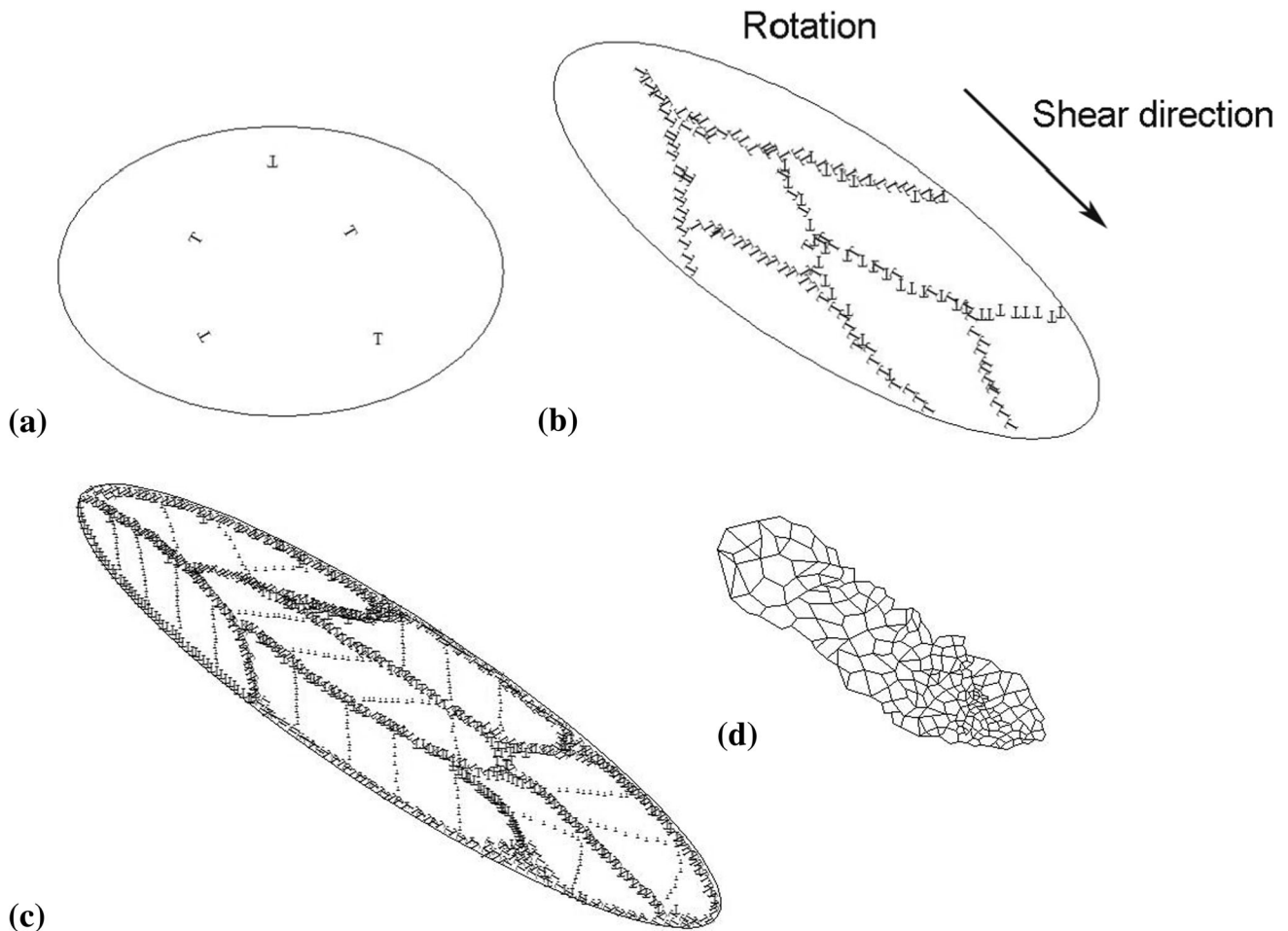


Fig. 9 The schematic diagram about the effect of shear strain on the microstructure evolution during adiabatic shearing. (a) original grain, (b) at a certain nominal shear strain (e.g., 2.0), grains within shear region elongated along the shear deformation, and the dislocation density increased and dislocation tangle or cell formed within grain. (c) at large shear strain (e.g., 3.6), grains were elongated and rotated into high-angle sub-grains, meanwhile dislocations and dislocation tangles produced within these sub-grains, and the process repeated as the shearing continuing. (d) as the shear strain further increases (e.g., 4.4), the sub-grains within ASB were refined into equiaxed nano-grains

nominal shear strain (e.g., up to 3.6), the sub-grains were formed from dislocation cells, and then the sub-grains were elongated with high dislocation density produced within them. When the nominal shear strain reached 4.4, the adiabatic shear deformation was still continuing; high density dislocation and dislocation tangle were produced within sub-grains, and then those sub-grains transform into high-angle sub-grains by rotation. The above process was finally finished in the progress of dynamic recrystallization (in Fig. 9).

4. Conclusion

- (1) The hat-shaped specimens with different thickness of stop ring were loaded at the same condition of dynamic deformation, which made the hat-shaped specimens locate in three stages of adiabatic shearing: the initial stage, the development period, and the maturity period, respectively. The ASB had not yet formed when the nominal shear strain was 2.0, while the widths of ASB with nominal shear strain of 3.6 and 4.4 were 15.4 and 18.7 μm , respectively.
- (2) When the nominal shear strain was 3.6 and 4.4, the average strain rate reached 5.0×10^5 and $5.2 \times 10^5/\text{s}^{-1}$, the true stress reached 1205 and 1402 MPa, and the adiabatic temperature rise were 954 and 985 K, respectively. RDR kinetics calculation showed that subgrains had sufficient time to generate an equiaxed microcrystalline structure by rotation within the deformation time.
- (3) As the shear strain increased, the grains in shear region were gradually elongated, dislocation density increased and sub-grains formed, and the sub-grains formed into high-angle sub-grains by rotation and eventually the nano-grains (100 nm) were formed. A model of the microstructure evolution during adiabatic shear localization was established, which concerned the effect of the shear strain on the adiabatic shear deformation.

Acknowledgments

This work is supported by the National Natural Science Foundation of China (No. 51274245), NSAF (No. U1330126), the Ph.D. Programs Foundation of Ministry of Education of China (No. 20120162130006), the key project of State Key Laboratory of Explosion Science and Technology (No. KFJJ11-1), and the Natural Science Fund of Hunan (No. 14 jj2011).

References

1. Q. Xue, J.F. Bingert, B.L. Henrie, and G.T. Gray, III, EBSD characterization of dynamic shear band regions in pre-shocked and as-received 304 stainless steels, *Mater. Sci. Eng. A*, 2008, **473**(1-2), p 279–289
2. M.A. Meyers, *Dynamic behavior of materials*, 1st ed., Wiley, New York, 1994, p 1–19
3. Y. Yang and B.F. Wang, Dynamic recrystallization in adiabatic shear band in α -titanium, *Mater. Lett.*, 2006, **60**(17-18), p 2198–2202
4. B.F. Wang and Y. Yang, Microstructure evolution in adiabatic shear band in fine-grain-sized Ti-3Al-5Mo-4.5V alloy, *Mater. Sci. Eng. A*, 2008, **473**(1-2), p 306–311
5. Y. Yang, F. Jiang, B.M. Zhou, X.M. Li, H.G. Zheng, and Q.M. Zhang, Microstructural characterization and evolution mechanism of adiabatic shear band in a near beta-Ti alloy, *Mater. Sci. Eng. A*, 2011, **528**(6), p 2787–2794
6. Y. Yang, Y. Zeng, D.H. Li, and M. Li, Damage and fracture mechanism of aluminium alloy thick-walled cylinder under external explosive loading, *Mater. Sci. Eng. A*, 2008, **490**(1-2), p 378–384
7. E. El-Magd and M. Abouridouane, Characterization, modelling and simulation of deformation and fracture behaviour of the light-weight wrought alloys under high strain rate loading, *Int. J. Impact Eng.*, 2006, **32**(5), p 741–758
8. M.A. Meyers, Y.B. Xu, Q. Xue, M.T. Perez-Prado, and T.R. McNelley, Microstructural evolution in adiabatic shear localization in stainless steel, *Acta Mater.*, 2003, **51**(5), p 1307–1325
9. Q. Xue and G.T. Gray, III, Development of adiabatic shear bands in annealed 316L stainless steel: part I. Correlation between evolving microstructure and mechanical behavior, *Metall. Mater. Trans. A*, 2006, **37**(8), p 2435–2446
10. J.F.C. Lins, H.R.Z. Sandim, H.J. Kestenbach, D. Raabe, and K.S. Vecchio, A microstructural investigation of adiabatic shear bands in an interstitial free steel, *Mater. Sci. Eng. A*, 2007, **457**(1-2), p 205–218
11. U. Andrade, M.A. Meyers, K.S. Vecchio, and A.H. Chokshi, Dynamic recrystallization in high-strain, high-strain-rate plastic deformation of copper, *Acta Metall. et Mater.*, 1994, **42**(9), p 3183–3195
12. D.H. Li, Y. Yang, T. Xu, H.G. Zheng, Q.S. Zhu, and Q.M. Zhang, Observation of the microstructure in the adiabatic shear band of 7075 aluminum alloy, *Mater. Sci. Eng. A*, 2010, **527**(15), p 3529–3535
13. Q. Xue, E.K. Cerreta, and G.T. Gray, III, Microstructural characteristics of post-shear localization in cold-rolled 316L stainless steel, *Acta Mater.*, 2007, **55**(2), p 691–704
14. Q. Xue and G.T. Gray, III, Development of adiabatic shear bands in annealed 316L stainless steel: part II. TEM studies of the evolution of microstructure during deformation localization, *Metall. Mater. Trans. A*, 2006, **37**(8), p 2447–2458
15. J.A. Hines and K.S. Vecchio, Recrystallization kinetics within adiabatic shear bands, *Acta Mater.*, 1997, **45**(2), p 635–649
16. R.S. Culver, *Thermal instability strain in dynamic plastic deformation, metallurgical effects at high strain rates*, Springer, New York, 1973, p 519–530
17. H. Wu, Z. Zeng, N. Guo, X. Zhang, T. Lei, and J. Han, Experimental study on the current loss of MITL With cathode made of different stainless steel, *IEEE Trans. Plast. Mater. Sci.*, 2012, **40**(4), p 1177–1182